
URDF-Anything+: Autoregressive Articulated 3D Models Generation for Physical Simulation

Zhuangzhe Wu¹ Yue Xin¹ Chengkai Hou¹ Minghao Chen² Yaoxu Lyu¹ Jieyu Zhang³ Shanghang Zhang¹

Abstract

Articulated objects are fundamental for robotics, simulation of physics, and interactive virtual environments. However, reconstructing them from visual input remains challenging, as it requires jointly inferring both part geometry and kinematic structure. We present *URDF-Anything+*, an end-to-end autoregressive framework that directly generates executable articulated object models from visual observations. Given image and object-level 3D cues, our method sequentially produces part geometries and their associated joint parameters, resulting in complete URDF models without reliance on multi-stage pipelines. The generation proceeds until the model determines that all parts have been produced, automatically inferring complete geometry and kinematics. Building on this capability, we enable a new Real-Follow-Sim paradigm, where high-fidelity digital twins constructed from visual observations allow policies trained and tested purely in simulation to transfer to real robots without online adaptation. Experiments on large-scale articulated object benchmarks and real-world robotic tasks demonstrate that *URDF-Anything+* outperforms prior methods in geometric reconstruction quality, joint parameter accuracy, and physical executability. Our project page is available at: <https://urdf-anything-plus.github.io/>

1. Introduction

Generating 3D object representations from visual observations is a fundamental challenge in spatial and embodied intelligence. While recent 3D generative models achieve high geometric fidelity, they typically output monolithic, unstructured shapes that lack internal decomposition (Chen

et al., 2025a;b; Gao et al., 2024; Melas-Kyriazi et al., 2024; Siddiqui et al., 2024; Wu et al., 2023; Pan et al., 2023). However, many real-world applications, such as robotic manipulation, physics-based simulation, and interactive virtual environments, demand compositional and functional representations, where objects are explicitly decomposed into parts with well-defined kinematic relationships (Chen et al., 2024; Li et al., 2025b; Le et al., 2025; Mandi et al., 2025). Building such articulated models in formats like URDF or XML is still largely a manual process, and automatic reconstruction from visual input remains challenging because it requires joint inference over part geometry and kinematic structure. Existing approaches often resort to multi-stage pipelines, retrieval from pre-built asset libraries, or reliance on explicit part segmentation (Chen et al., 2024; Le et al., 2025).

In this paper, we propose **URDF-Anything+**, an end-to-end framework for generating fully functional articulated URDF models directly from visual observations. Given an image and object-level 3D geometry, URDF-Anything+ outputs both link geometries and their associated joint parameters in a part-by-part autoregressive manner, producing physically executable models that can be directly deployed in standard simulation. This enables a unified perception-to-simulation pipeline, supporting scalable digital twin construction, free-form articulated object generation and robotic learning.

Our approach is motivated by the observation that articulated objects are inherently compositional and are naturally modeled through autoregressive generation. Inspired by AutoPartGen (Chen et al., 2025b), URDF-Anything+ adopts an autoregressive diffusion-based formulation and extends it to jointly generate part geometry and joint parameters. Each part is represented using a continuous latent 3D representation based on 3DShape2VecSet (Zhang et al., 2023). Operating in this structured latent space, URDF-Anything+ sequentially generates articulated objects, predicting both geometry and articulation at each step to ensure consistent shape and kinematics.

To demonstrate the effectiveness of URDF-Anything+, we introduce a new framework named Real-Follow-Sim, which uses visual observations to build a digital twin of the physical environment. In this framework, we learn the robotic

¹State Key Laboratory of Multimedia Information Processing, School of Computer Science, Peking University ²Visual Geometry Group, University of Oxford ³University of Washington. Correspondence to: Shanghang Zhang <shanghang@pku.edu.cn>.

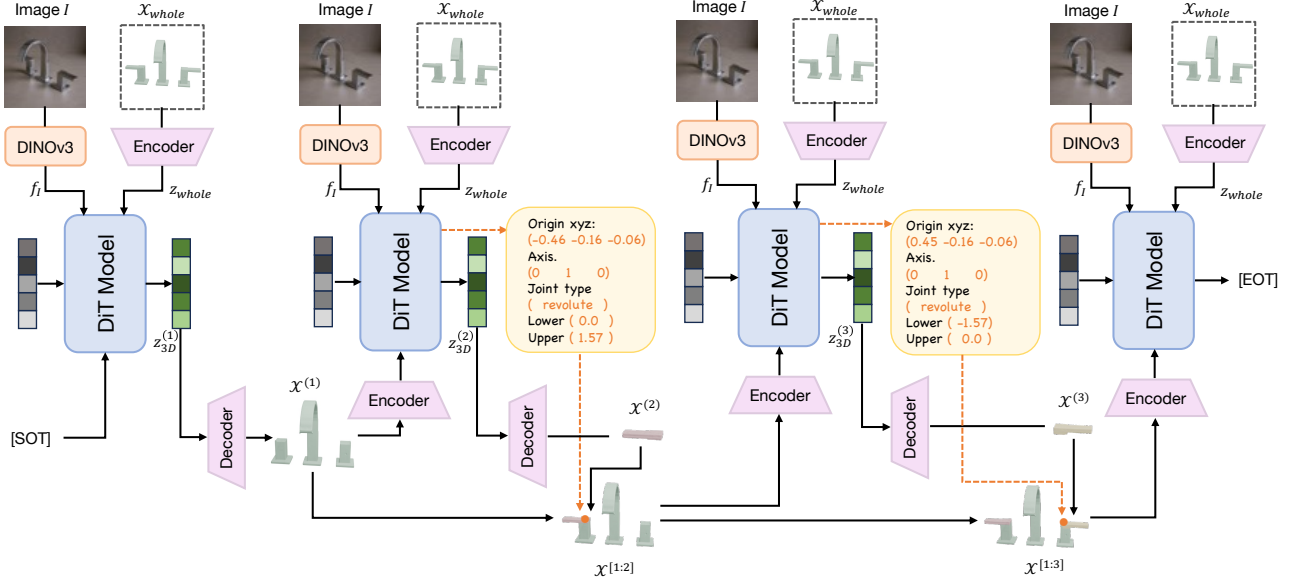


Figure 1. Overview of the URDF-Anything Generation Pipeline. It shows how we autoregressively generate the 3D components of an object along with their spatial configurations using a DiT model, and then assemble them into a complete URDF file.

policies entirely within this high-fidelity simulation and directly execute the learned policy in the real world without online adaptation. Unlike conventional Sim-to-Real (Sim2Real) (Wagenmaker et al., 2024; Chukwurah et al., 2024; Chen et al., 2021) approaches that assume a fixed simulator with hand-crafted or simplified assets, forcing policies to compensate for modeling errors and often limiting generalization to novel scenes and articulated objects, Real-Follow-Sim enables the simulator itself to adapt to the real world through on-demand reconstruction of articulated object models. By shifting the burden of realism from policy generalization to simulation fidelity, our system enables seamless zero-shot transfer of complex manipulation skills.

We validate URDF-Anything+ and Real-Follows-Sim on large-scale articulated object benchmarks and real-world robotic tasks. Our method significantly outperforms prior approaches in both geometric reconstruction and joint parameter prediction and yields a substantially higher rate of physically executable URDFs, even for challenging objects outside the training distribution.

In general, our contributions are threefold: (i) we introduce URDF-Anything+, a unified autoregressive diffusion framework to generate fully functional articulated URDF models from images or 3D geometry. (ii) we present Real-Follows-Sim, which uses URDF-Anything+ for digital twin construction and zero-shot simulation-to-real policy transfer. (iii) We conduct extensive experiments demonstrating state-of-the-art performance in geometry, joint accuracy and physical executability across synthetic and real datasets.

2. Related Work

3D Generation Method. Researchers have developed strong geometric priors for synthesizing shapes from text, images, or multi-view observations, enabling scalable reconstruction and synthesis of 3D content. Single-image-to-3D generation addresses the challenge of recovering full 3D geometry from sparse visual input (Xu et al., 2024; Li et al., 2025a; Hong et al., 2024; Zhang et al., 2024a; Liu et al., 2023b; 2024b; 2023c; 2024c). Beyond optimization-based pipelines, generative 3D models explore alternative representations and latent structures, including implicit generative models such as Shap-E (Jun & Nichol, 2023) and GET3D (Gao et al., 2022), as well as structured latent formulations exemplified by Trellis (Xiang et al., 2025b;a) and CLAY (Zhang et al., 2024b). Gaussian-based 3D generation further improves efficiency and rendering quality through explicit point-based representations (Tang et al., 2024; Yi et al., 2024). Complementary to holistic shape synthesis, part-level 3D generation explicitly models semantic parts to improve controllability and compositionality, through either diffusion-based multi-view part reconstruction or autoregressive part generation and discovery (Chen et al., 2025a;b).

Articulated Object Models. Currently, they focus on recovering part decomposition, kinematic structure, and motion constraints of human-made objects from visual observations, forming a foundation for robotic interaction and simulation (Liu et al., 2025b). Early work primarily studied articulated structure inference from 3D geometry or partial observations, supported by part-level benchmarks and interactive simulation platforms such as PartNet (Mo et al., 2019)

and SAPIEN (Xiang et al., 2020). These efforts explored generalizable kinematic modeling, movable or openable part detection, part-level pose estimation, and articulated shape representation, including self-supervised category-level articulation learning and disentangled implicit formulations (Abbatematteo et al., 2020; Jiang et al., 2022; Liu et al., 2023a;d; Mu et al., 2021). Subsequent approaches shift toward vision-conditioned and controllable modeling, leveraging visual input to recover articulated structure directly from images, including neural implicit representations for articulated digital twins and vision- or vision-language-based articulation reasoning (Weng et al., 2024; Le et al., 2025; Chen et al., 2024; Liu et al., 2025a; 2024a). Alongside vision-conditioned articulation modeling, growing attention has been directed toward generating simulation-ready articulated assets with executable representations, including code-based reconstruction of articulated objects (Mandi et al., 2025), symbolic URDF construction via multimodal language models (Li et al., 2025b), and physically grounded asset synthesis compatible with physics engines (Cao et al., 2025b).

3. Method

Given a single RGB image, our goal is to infer a complete articulated object model that explicitly represents part geometries and their kinematic relationships. The output is a valid URDF (Unified Robot Description Format) file that can be directly instantiated in standard physics simulators, enabling downstream robot policy learning without manual asset engineering.

Starting from the input image, URDF-Anything+ first reconstructs a complete 3D model at the object-level and then autoregressively decomposes it into rigid links together with their articulation parameters. Specifically, we extract visual features using a pretrained DINOv3 encoder (Siméoni et al., 2025) and reconstruct the full object geometry using TripoSG (Li et al., 2025a). Based on these global visual and geometric cues, our model sequentially generates part-level geometries and their associated joint specifications, including joint type, axis, origin, and limits. The predicted components are finally assembled into a fully specified URDF model.

3.1. Task Definition

Let $\mathcal{X}_{\text{whole}}$ denote the complete object-level 3D geometry capturing the external appearance of an articulated object, typically represented as a single mesh. Importantly, $\mathcal{X}_{\text{whole}}$ does not necessarily coincide with the union of its part-level geometries, as articulated parts may contain internal or functional structures that are not directly observable from the exterior surface.

An articulated object is represented by

$$\mathcal{A} = (\{\mathcal{X}^{(k)}\}_{k=1}^K, \{\mathcal{J}^{(k)}\}_{k=1}^K), \quad (1)$$

where $\mathcal{X}^{(k)}$ denotes the mesh of the k -th rigid link and $\mathcal{J}^{(k)}$ specifies the joint parameters defining the kinematic relationship between part $\mathcal{X}^{(k)}$ and its parent. Each $\mathcal{J}^{(k)}$ includes the joint type, axis, origin, and motion limits. Together, these components define a URDF model that can be directly instantiated in a physics simulator.

We consider the image-to-articulated-model setting, where the input consists of a single RGB image I . From I , we first reconstruct a complete object-level geometry $\mathcal{X}_{\text{whole}}$ using a pretrained reconstruction model. The task is then to infer a plausible articulated representation \mathcal{A} conditioned on both the visual observation and the reconstructed geometry, i.e. $(I, \mathcal{X}_{\text{whole}}) \rightarrow \mathcal{A}$

Recovering articulated structure from visual input is inherently ambiguous. We therefore model the problem as learning a conditional distribution

$$p(\{\mathcal{X}^{(k)}\}_{k=1}^K, \{\mathcal{J}^{(k)}\}_{k=1}^K \mid I, \mathcal{X}_{\text{whole}}), \quad (2)$$

from which valid articulated URDF models can be sampled for downstream real-to-sim-to-real policy learning.

3.2. Latent 3D Shape Modeling via Diffusion

Directly modeling probability distributions over continuous 3D surfaces is intractable due to their infinite-dimensional nature. We therefore adopt a finite-dimensional latent representation and perform generative modeling in this structured latent space.

We represent 3D geometry using the *VecSet* formulation (Zhang et al., 2023) which learns an encoder-decoder pair (E, D) , where E and D denote the encoder and decoder networks respectively. Given a surface \mathcal{X} , the encoder maps an N -point cloud $\mathcal{P} = \{\mathbf{p}_i \in \mathbb{R}^3\}_{i=1}^N \subseteq \mathcal{X}$ to a compact latent representation $\mathbf{z} = E(\mathcal{P}) = (z_1, \dots, z_M) \in \mathbb{R}^{M \times D}$, where $M \ll N$ and each z_i is a D -dimensional feature vector. The encoder E is implemented as a permutation-equivariant transformer that subsamples points and aggregates global context via cross-attention. The decoder D evaluates the signed distance function by mapping a query point $\mathbf{p} \in \mathbb{R}^3$ and the latent tokens \mathbf{z} to $\text{SDF}(\mathbf{p} \mid \mathcal{X}) = D(\mathbf{p} \mid \mathbf{z})$, using a Perceiver-style architecture (Jaegle et al., 2021). This provides a continuous implicit representation of the 3D shape.

To generate shapes conditioned on visual evidence y (e.g., an input image), we learn a conditional distribution $p(\mathbf{z} \mid y)$ using latent diffusion. We define a forward noising process

$$\mathbf{z}_t = \sqrt{\bar{\alpha}_t} \mathbf{z} + \sqrt{1 - \bar{\alpha}_t} \epsilon, \quad \epsilon \sim \mathcal{N}(0, I), \quad (3)$$

with a predefined noise schedule $\{\alpha_t\}_{t=0}^T$ and $\bar{\alpha}_t = \prod_{s=1}^t \alpha_s$. Following (Song et al., 2021), we parameterize the diffusion process via the flow velocity

$$\mathbf{v}(t, \mathbf{z}_0, \epsilon) = \sqrt{\bar{\alpha}_t} \epsilon - \sqrt{1 - \bar{\alpha}_t} \mathbf{z}_0. \quad (4)$$

A neural network $\hat{\mathbf{v}}_\theta(\mathbf{z}_t, t \mid y)$ is trained to predict the velocity at diffusion step t , conditioned on the noised latent \mathbf{z}_t and the input evidence y .

$$\mathcal{L}_{diff} = \mathbb{E}_{y, \mathbf{z}, t, \epsilon} \left\| \hat{\mathbf{v}}_\theta(t, \mathbf{z}_t \mid y) - \mathbf{v}(t, \mathbf{z}_0, \epsilon) \right\|^2. \quad (5)$$

After training, the model can sample latent shape representations consistent with the input evidence, which are then decoded into 3D geometry.

3.3. Autoregressive Articulated Model Generation

Our articulated model generation follows the compositional autoregressive paradigm introduced in AutoPartGen (Chen et al., 2025b), while extending it to jointly synthesize part geometry and articulation parameters within a unified diffusion-based framework. Fig. 1 provides an overview of the generation process.

Problem Formulation. Given an input image I , we extract image features f_I using DINOv3 and reconstruct a complete object mesh $\mathcal{X}_{\text{whole}}$ via TripoSG (Li et al., 2025a). The reconstructed mesh is encoded into a global 3D latent $\mathbf{z}_{\text{whole}} = E(\mathcal{X}_{\text{whole}})$. The pair $(f_I, \mathbf{z}_{\text{whole}})$ serves as global context for autoregressive generation.

At each autoregressive step k , the model generates a single articulated part represented by the tuple $(\mathbf{z}_{3D}^{(k)}, \mathcal{J}^{(k)})$, where $\mathbf{z}_{3D}^{(k)}$ is a latent code representing the geometry of the k -th part and $\mathcal{J}^{(k)}$ denotes its articulation parameters. Given conditioning inputs (image features f_I and complete object 3D latent $\mathbf{z}_{\text{whole}}$) and the context accumulated from previously generated parts ($\mathbf{z}_{\text{pre}}^{[1:k-1]}$, defined at 7), the overall generation process is modeled as

$$p\left(\mathbf{z}_{3D}^{(k)}, \mathcal{J}^{(k)} \mid f_I, \mathbf{z}_{\text{whole}}, \mathbf{z}_{\text{pre}}^{[1:k-1]}\right). \quad (6)$$

Re-encoding and Autoregressive Context Update. After decoding the k -th part, we merge it with previously generated geometry: $\mathcal{X}^{[1:k]} = \bigcup_{j=1}^k \mathcal{X}^{(j)}$. Following AutoPartGen (Chen et al., 2025b), we sample surface points from the merged geometry and re-encode it to update the context:

$$\mathbf{z}_{\text{pre}}^{[1:k]} = E\left(\text{sample } \mathcal{X}^{[1:k]}\right). \quad (7)$$

This re-encoding step ensures that the context used for subsequent generation reflects the actual decoded geometry rather than latent concatenations alone.

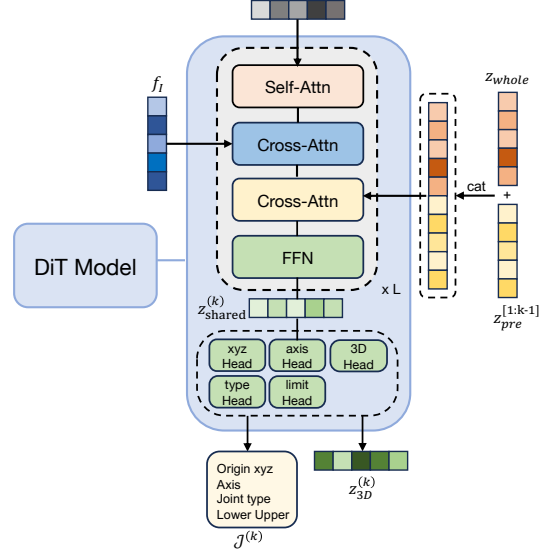


Figure 2. Structure of DiT and parameter decoders.

Latent Diffusion with Shared Latent. Part generation is driven by a diffusion transformer (DiT) operating in latent space. At step k , the DiT takes a noisy latent \mathbf{z}_t together with conditioning tokens derived from y and $\mathbf{z}_{\text{pre}}^{[1:k-1]}$, and predicts a denoising velocity field. At the final diffusion step ($t = 0$), the model produces a *shared latent*

$$\mathbf{z}_{\text{shared}}^{(k)} = f_{\text{DiT}}\left(f_I, \mathbf{z}_{\text{whole}}, \mathbf{z}_{\text{pre}}^{[1:k-1]}\right), \quad (8)$$

which aggregates global geometric structure and contextual information for the current part.

Geometry Latent and 3D Decoding. The geometry latent of the k -th part is obtained by projecting the shared latent through a dedicated 3D head: $\mathbf{z}_{3D}^{(k)} = h_{3D}\left(\mathbf{z}_{\text{shared}}^{(k)}\right)$. We then reconstruct the part geometry using the TripoSG decoder D : $\mathcal{X}^{(k)} = D\left(\mathbf{z}_{3D}^{(k)}\right)$.

Articulation Parameter Decoding. Articulation parameters are predicted deterministically from the shared latent. We employ multiple lightweight MLP heads, each responsible for a specific joint attribute:

$$\mathbf{o}^{(k)} = h_{\text{orig}}\left(\mathbf{z}_{\text{shared}}^{(k)}\right), \quad (9)$$

$$\mathbf{a}^{(k)} = h_{\text{axis}}\left(\mathbf{z}_{\text{shared}}^{(k)}\right), \quad (10)$$

$$\ell_{\text{low}}^{(k)}, \ell_{\text{up}}^{(k)} = h_{\text{low, up}}\left(\mathbf{z}_{\text{shared}}^{(k)}\right), \quad (11)$$

$$\tau^{(k)} = h_{\text{type}}\left(\mathbf{z}_{\text{shared}}^{(k)}\right), \quad (12)$$

We denote the complete articulation specification as $\mathcal{J}^{(k)} = (\mathbf{o}^{(k)}, \mathbf{a}^{(k)}, \tau^{(k)}, \ell_{\text{low}}^{(k)}, \ell_{\text{up}}^{(k)})$. Conditioning articulation prediction on the shared latent allows joint parameters to leverage global context captured during diffusion, leading to

geometrically consistent articulation. Fig. 2 shows the DiT and parameter decoder’s structure.

Overall Perspective. By iterating over shared-latent diffusion, geometry decoding, articulation prediction, mesh merging, and re-encoding, the proposed framework incrementally constructs a complete articulated object. This design preserves the compositional strengths of AutoPartGen while enabling coherent, end-to-end generation of URDF-ready articulated models.

4. Real-Follow-Sim

Traditional Sim-to-Real approaches suffer from a significant domain gap between simulation and the real world. Thus, the trained policy has to be able to generalize across this gap, forcing the neural network to “guess” the true dynamics of the physical environment despite imperfect or simplified simulators. This places an immense burden on the learning algorithm, leading to high training costs, brittle real-world performance, and frequent failures during deployment.

In contrast, we propose **Real-Follow-Sim**, a paradigm that shifts the primary challenge from policy generalization to simulation fidelity. We construct a dynamic digital twin of the real environment by leveraging URDF-Anything+ to stream real-world visual observations into the simulator, thereby continuously aligning the virtual scene with its physical counterpart in both geometry and appearance. Crucially, the policy is trained and executed exclusively in simulation, operating solely on synthetic data. The real robot acts merely as a faithful “follower”, executing the actions generated by the simulated agent without any online adaptation. Overall, our framework consists of three stages: (1) Digital Twin Asset Construction; (2) Policy Learning in Simulation; (3) Real-World Execution via Simulated Trajectories.

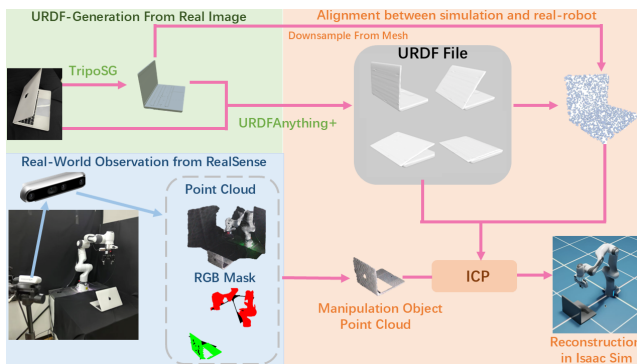


Figure 3. Pipeline for Real-to-Sim Digital Twin Construction. Our system captures RGB-D data from the real world, generates articulated URDF models using URDF-Anything+, aligns them with observed geometry via ICP, scales them to physical size, and instantiates them in Isaac Sim to create a spatially accurate digital twin.

Digital Twin Asset Construction. We present a pipeline for digital twin asset construction that bridges real-world scenes and physics-based simulation. Using an Intel RealSense camera, we capture synchronized RGB-D data from a physical environment. The 3D point cloud is first segmented into individual object instances by leveraging color coherence. We then crop the 2D image of the object manipulated by the robotic arm and feed it into the URDF-Anything+ to obtain its URDF file. Next, we sample a point cloud from the generated mesh by TripoSG (Li et al., 2025a), and align it with the point cloud segmented from the real-world scene using ICP (Besl & McKay, 1992). We scale the original URDF File to match the actual physical size of the object based on this alignment. Finally, the URDF models are instantiated in Isaac Sim at their estimated world-frame poses from the camera, establishing a spatially aligned digital twin that accurately mirrors the real scene and enables realistic robot policy evaluation and transfer. Fig. 3 shows the pipeline for Real-to-Sim digital twin construction.

Policy Learning in Simulation. After accurately replicating the real-world scene in simulation, we collect task-relevant data in Isaac Sim, which captures both proprioceptive signals (such as joint states and motion trajectories of the robot) and 2D visual observations during task execution. Data are generated by executing expert trajectories in simulation, where object poses and scene configurations can be easily randomized. This enables efficient collection of diverse demonstrations covering a wide range of initial conditions. For each object category, we define a single expert policy that demonstrates the intended manipulation behavior.

Real-World Execution via Simulated Trajectories. In the real robotic deployment, we directly instantiate a simulation environment that faithfully matches the real-world layout and object configuration. The policy trained entirely in simulation is then evaluated within this reconstructed scene. Crucially, the motion trajectories generated by the learning policy can be directly scaled and transferred to the real-world robot, enabling it to accurately reproduce the simulated behaviors in the real world. This enables us to transfer robot policies learned in simulation to real-world deployment without relying on any Sim-to-Real adaptation techniques.

5. Experiments

5.1. Implementation Details.

Training Details. We adopt a two-stage training strategy to stabilize learning and progressively introduce articulation-aware supervision. In **Stage 1**, the model is trained for 500 epochs on 16 NVIDIA A800 GPUs using only image

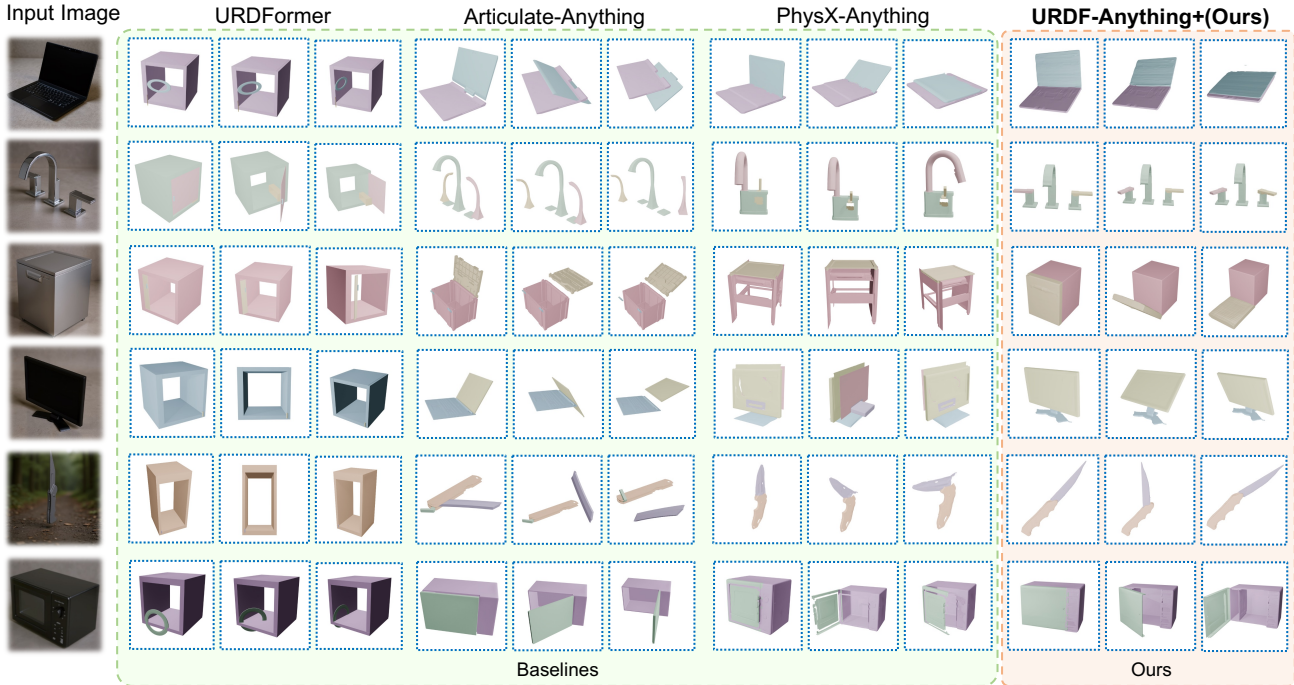


Figure 4. **Qualitative Results on the Test Set of Our Dataset.** Compared with other methods, URDF-Anything+ generates high-quality 3D assets with more accurate geometry and articulation.

and part-geometry supervision, excluding the end-of-token ($[E_{OT}]$) signal and URDF-based articulation annotations. This stage focuses on learning robust latent geometry representations and autoregressive part composition. In **Stage 2**, training continues for an additional 100 epochs with the $[E_{OT}]$ signal and URDF-based articulation annotations enabled, thereby introducing full articulation supervision. This stage allows the model to jointly learn part termination, articulation parameter prediction, and geometry generation in a unified framework. More details are reported at Appendix B.1 .

Training Data. Our training data is constructed from a curated collection of articulated 3D datasets, including PartNet (Mo et al., 2019), PartNet-Mobility, and PhysX3D (Cao et al., 2025a). We apply extensive data cleaning and filtering to ensure geometric validity and consistent articulation structure. Further implementation details are provided in supplementary material Section A .

5.2. Geometric Quality Evaluation

We compare URDF-Anything+ with the most relevant state-of-the-art methods on articulated 3D geometry generation, including URDFormer (Chen et al., 2024), Articulate-Anything (Le et al., 2025), and PhysX-Anything (Cao et al., 2025b). As shown in Table 1, URDF-Anything+ consistently

Table 1. **3D Part Completion.** Reconstruction quality of the parts and whole object. Average prediction errors for IoU & F-Score (Higher is better (\uparrow)), and CD (Lower is better (\downarrow)).

Method	Parts			Whole Object		
	IoU \uparrow	F-Score \uparrow	CD \downarrow	IoU \uparrow	F-Score \uparrow	CD \downarrow
URDFormer (Chen et al., 2024)	0.202	0.389	0.354	0.243	0.413	0.286
Articulate-Anything (Le et al., 2025)	0.563	0.452	0.064	0.627	0.510	0.053
Physx-Anything (Cao et al., 2025b)	0.784	0.697	0.076	0.813	0.715	0.068
URDF-Anything+(Ours)	0.879	0.721	0.033	0.930	0.742	0.009

tently achieves superior performance across all geometric metrics, including IoU, F-score, and Chamfer Distance (CD).

In particular, URDF-Anything+ attains the highest IoU and F-score while achieving the lowest CD, indicating more accurate surface reconstruction and better geometric completeness.

Compared to retrieval-based or single-pass generation methods, our approach better captures fine-grained part geometry and preserves global structural consistency across articulated components. We observe that PhysX-Anything and URDF-Anything+ achieve higher performance in geometric generation, as measured by IoU and F-score, which quantify the overlap between the generated geometry and the ground-truth shapes, compared to retrieval-based methods such as URDFormer and Articulate-Anything, which is consistent with our expectations.

5.3. Joint Parameter Prediction Accuracy.

Table 2. **Joint Parameter Prediction Accuracy.** Average prediction errors for joint Axis (rad), Origin (meters), and Limit(rad). Lower is better (\downarrow).

Method	Axis \downarrow	Origin \downarrow	Limit \downarrow
URDFormer(Chen et al., 2024)	1.071 \pm 0.497	0.504 \pm 0.331	0.882 \pm 0.679
Articulate-Anything (Le et al., 2025)	0.230 \pm 0.505	0.267 \pm 0.357	1.108 \pm 0.676
PhysX-Anything (Cao et al., 2025b)	0.191 \pm 0.337	0.103 \pm 0.192	0.532 \pm 0.423
URDF-Anything+ (Ours)	0.129\pm0.404	0.062\pm0.096	0.225\pm0.440

Following the evaluation protocol of Articulate-Anything (Le et al., 2025), we evaluate the accuracy of joint parameter prediction by comparing the predicted URDF parameters with ground-truth annotations. We focus on articulated objects with *revolute* joints and report errors on three key joint attributes: (1) **Joint Axis Error**, defined as the angular difference between the predicted and ground-truth joint axes, normalized to the range $[0, \pi]$; (2) **Joint Origin Error**, measured as the Euclidean distance between the predicted and ground-truth joint origins; and (3) **Joint Limit Error**, which quantifies the discrepancy between the predicted and ground-truth joint limits.

Table 2 presents the quantitative results. We compare URDF-Anything+ (Ours) with several prior methods on the same evaluation set. As shown in the table, URDF-Anything+ consistently achieves lower errors across all reported joint parameters. This indicates that our method can more accurately recover the kinematic configuration of articulated objects, particularly in terms of joint geometry and motion constraints.

These results demonstrate the effectiveness of our approach in predicting fine-grained joint parameters. We attribute the improved performance to our end-to-end framework, which couples autoregressive geometric generation with shared-latent articulation decoding. Beyond the quantitative comparison, we further present qualitative results in Fig.4 and Fig.5.

5.4. Ablation

Effect of Input Modalities. To validate our design choices, we study the effect of different input modalities on URDF-Anything+ using the *faucet* category, whose geometry is among the most complex across all object classes. This choice is motivated by the fact that faucets have complicated structures, making it particularly challenging to generate accurate geometry without explicit 3D whole-object guidance. All models are trained following the same two-stage protocol as the main setting: pretraining for 300 epochs without $[E_{OT}]$ or URDF supervision, followed by 100 epochs of fine-tuning with $[E_{OT}]$ and URDF parameter prediction enabled. The architecture and training schedule are kept identical across all variants, with differences only in the

available input modalities.

As shown in Table 3, using image input alone allows the model to infer articulation from visual cues but often results in ambiguities in fine-grained geometry and joint placement. Combining image and 3D inputs consistently achieves better performance across all evaluated metrics, including geometric quality and joint parameter accuracy.

Effect of Link Ordering. We study the impact of link ordering in the training data on articulated model generation using the refrigerator category, as a large portion of refrigerators consists of multiple articulated links. Specifically, we compare using a random permutation of links with a deterministic ordering based on the joint origin coordinates, where links are sorted by the (x, y, z) position of their associated joints in ascending order. The details are shown in Appendix Section A.4. Since our model follows an autoregressive generation paradigm, the ordering of links implicitly defines the factorization of the joint distribution. As shown in Table 3, the proposed spatially consistent ordering leads to more accurate geometry reconstruction and joint parameter prediction, indicating that a stable and physically meaningful ordering facilitates learning dependencies among articulated parts.

5.5. Real-World Experiment

We design several real-world robot tasks to implement the “**Real-Follow-Sim**” paradigm described in Section 4. We validate the effectiveness of our framework in real-world manipulation tasks using a Franka robotic arm with a Robotiq Gripper (Robotiq Inc., 2025). A Realsense camera (Intel Corporation, 2025) is mounted on the side of the robotic arm, providing a viewpoint similar to the ego-centric human video data used in the pre-visual model. For the real-robot tasks, we select two types of handover objects for robotic manipulation. The first task involves using a robotic arm to close a laptop lid, and the second task requires the robotic arm to push a drawer (see Figure 6).

In the experiments, we consistently use Diffusion Policy (Chi et al., 2025) for robot policy learning. For a fair comparison, both real-world and simulated datasets contain 50 demonstration episodes per task. Each task is evaluated in real-world scenarios with 20 trials, and task performance is measured by its success rate.

Real-Follow-Sim VS. Sim-to-Real. We compare our proposed approach, where the physical robot follows motion trajectories generated by the simulated robot, against the conventional paradigm of deploying policies trained in simulation directly onto real-world robots. The results are shown in Table 4, which illustrates that Real-Follow-Sim paradigm effectively addresses the Sim-to-Real gap by aligning the

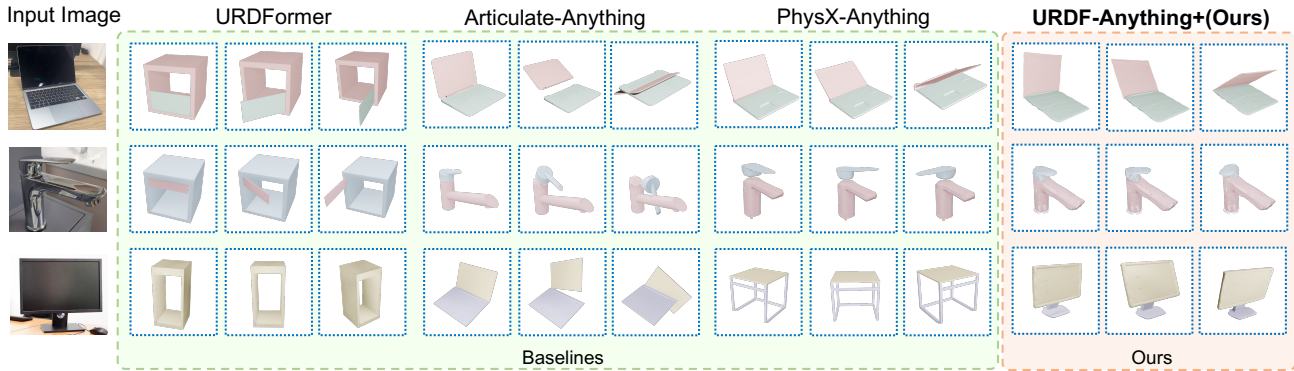


Figure 5. **Qualitative Results on Tn-the-wild Images.** Compared with other methods, URDF-Anything+ generates high-quality 3D assets with more accurate geometry and articulation.

Table 3. **Ablation Studies.** We evaluate the impact of input modalities (top) and link ordering strategies (bottom) on geometry reconstruction and joint prediction accuracy.

Objectives	Variation	Geometry Quality						Joint Accuracy		
		Parts			Whole Object			Axis Err. ↓	Origin Err. ↓	Limit ↓
		IoU ↑	F-Score ↑	CD ↓	IoU ↑	F-Score ↑	CD ↓			
Input Modality	Image Only	0.627	0.560	0.106	0.682	0.634	0.098	0.349	0.197	0.540
	Image + 3D Guid.(Ours)	0.823	0.740	0.028	0.841	0.766	0.009	0.182	0.091	0.281
Link Ordering	Random Order	0.630	0.686	0.145	0.710	0.704	0.072	0.203	0.168	0.442
	Order by Joint XYZ (Ours)	0.805	0.742	0.096	0.816	0.753	0.034	0.120	0.102	0.323

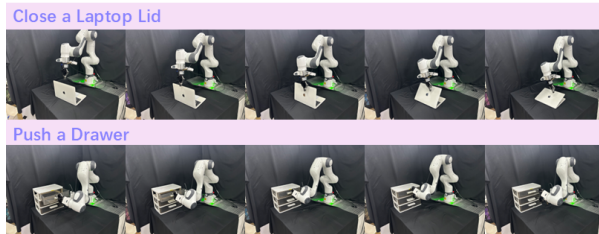


Figure 6. **Visualization of real-world tasks.**

simulation with the real world.

Comparison with Other Baselines Performance. We compare the real-world performance of different URDF generation methods within our proposed Real-Follow-Sim framework. Table 4 shows that URDF-Anything+ outperforms Articulate-Anything in real-world robot performance.

Comparison with Real Data Training. In this section, we primarily compare the real-world performance of two policy training paradigms: (1) policies trained on a dataset collected directly on the real-world robot using a fixed amount of real-world data. (2) policies trained entirely in simulation using an equally sized dataset generated efficiently under our Real-Follow-Sim framework.

Following the Table 4, we find that our method outperforms URDF generation baselines, improves over the standard Sim-to-Real deployment paradigm, and enables simulation-

Table 4. **Real-World performance evaluation.** We compare our method across different deployment paradigms, URDF generation baselines, and training data sources. Success rates (%) are reported.

Method / Setting	Close Laptop	Close Drawer
<i>Comparison of deployment paradigms</i>		
Sim-to-Real	80	75
Real-Follow-Sim (Ours)	100	90
<i>Comparison of URDF generation methods (under Real-Follow-Sim)</i>		
Articulate-Anything	75	55
URDF-Anything+ (Ours)	100	90
<i>Comparison of training data sources</i>		
Real-Only	85	75
Simulation-Only (Ours)	100	90

only training to achieve strong real-world performance. These results show the effectiveness of Real-Follow-Sim as a unified framework for real-world manipulation.

6. Conclusion

We present **URDF-Anything+**, an end-to-end framework generating physically articulated URDFs directly from visual observations, significantly outperforming prior methods in both geometry and kinematic accuracy. Built upon this, we introduce the **Real-Follow-Sim** paradigm: using URDF-Anything+ to construct high-fidelity digital twins of real environments; policies trained purely in simulation can be deployed on physical robots with minimal online adaptation.

Impact Statement

This paper presents work whose goal is to advance the field of robotic manipulation and articulated object modeling. There are many potential societal consequences of this work, none of which we feel must be specifically highlighted here.

References

- Abbatematteo, B., Tellex, S., and Konidaris, G. Learning to generalize kinematic models to novel objects. In Kaelbling, L. P., Kragic, D., and Sugiura, K. (eds.), *Proceedings of the Conference on Robot Learning*, volume 100 of *Proceedings of Machine Learning Research*, pp. 1289–1299. PMLR, 2020.
- Besl, P. J. and McKay, N. D. Method for registration of 3-d shapes. In *Sensor fusion IV: control paradigms and data structures*, volume 1611, pp. 586–606. Spie, 1992.
- Cao, Z., Chen, Z., Pan, L., and Liu, Z. Physx-3d: Physical-grounded 3d asset generation. *arXiv preprint arXiv:2507.12465*, 2025a.
- Cao, Z., Hong, F., Chen, Z., Pan, L., and Liu, Z. Physx-anything: Simulation-ready physical 3d assets from single image. *arXiv preprint arXiv:2511.13648*, 2025b.
- Chen, M., Shapovalov, R., Laina, I., Monnier, T., Wang, J., Novotny, D., and Vedaldi, A. Partgen: Part-level 3d generation and reconstruction with multi-view diffusion models. In *Proceedings of the Computer Vision and Pattern Recognition Conference*, pp. 5881–5892, 2025a.
- Chen, M., Wang, J., Shapovalov, R., Monnier, T., Jung, H., Wang, D., Ranjan, R., Laina, I., and Vedaldi, A. Autopartgen: Autoregressive 3D part generation and discovery. In *Proceedings of the 39th Annual Conference on Neural Information Processing Systems (NeurIPS)*, 2025b.
- Chen, X., Hu, J., Jin, C., Li, L., and Wang, L. Understanding domain randomization for sim-to-real transfer. *arXiv preprint arXiv:2110.03239*, 2021.
- Chen, Z. Q., Walsman, A., Memmel, M., Mo, K., Fang, A., Vemuri, K., Wu, A., Fox, D., and Gupta, A. Urdformer: A pipeline for constructing articulated simulation environments from real-world images. *CoRR*, abs/2405.11656, 2024.
- Chi, C., Xu, Z., Feng, S., Cousineau, E., Du, Y., Burchfiel, B., Tedrake, R., and Song, S. Diffusion policy: Visuomotor policy learning via action diffusion. *The International Journal of Robotics Research*, 44(10-11): 1684–1704, 2025.
- Chukwurah, N., Adebayo, A. S., and Ajayi, O. O. Sim-to-real transfer in robotics: Addressing the gap between simulation and real-world performance. *International Journal of Robotics and Simulation*, 6(1):89–102, 2024.
- Gao, J., Shen, T., Wang, Z., Chen, W., Yin, K., Li, D., Litany, O., Gojcic, Z., and Fidler, S. Get3d: A generative model of high quality 3d textured shapes learned from images. *Advances in neural information processing systems*, 35: 31841–31854, 2022.
- Gao, R., Holynski, A., Henzler, P., Brussee, A., Martin-Brualla, R., Srinivasan, P., Barron, J. T., and Poole, B. Cat3d: Create anything in 3d with multi-view diffusion models. *arXiv preprint arXiv:2405.10314*, 2024.
- Hong, Y., Zhang, K., Gu, J., Bi, S., Zhou, Y., Liu, D., Liu, F., Sunkavalli, K., Bui, T., and Tan, H. Lrm: Large reconstruction model for single image to 3d. In *International Conference on Learning Representations (ICLR)*, 2024.
- Intel Corporation. Intel@realsense™lidar camera 1515. <https://www.intelrealsense.com/lidar-camera-1515/>, 2025. Accessed: 2025-02-01.
- Jaegle, A., Borgeaud, S., Alayrac, J.-B., Doersch, C., Ionescu, C., Ding, D., Koppula, S., Zoran, D., Brock, A., Shelhamer, E., et al. Perceiver io: A general architecture for structured inputs & outputs. *arXiv preprint arXiv:2107.14795*, 2021.
- Jiang, H., Mao, Y., Savva, M., and Chang, A. X. Opd: Single-view 3d openable part detection. In *European Conference on Computer Vision*, pp. 410–426. Springer, 2022.
- Jun, H. and Nichol, A. Shap-e: Generating conditional 3d implicit functions. *arXiv preprint arXiv:2305.02463*, 2023.
- Le, L., Xie, J., Liang, W., Wang, H.-J., Yang, Y., Ma, Y. J., Vedder, K., Krishna, A., Jayaraman, D., and Eaton, E. Articulate-anything: Automatic modeling of articulated objects via a vision-language foundation model. In *The Thirteenth International Conference on Learning Representations*, 2025.
- Li, Y., Zou, Z.-X., Liu, Z., Wang, D., Liang, Y., Yu, Z., Liu, X., Guo, Y.-C., Liang, D., Ouyang, W., and Cao, Y.-P. Triposg: High-fidelity 3d shape synthesis using large-scale rectified flow models. In *Proceedings of the IEEE/CVF International Conference on Computer Vision (ICCV)*, 2025a.
- Li, Z., Bai, X., Zhang, J., Wu, Z., Xu, C., Li, Y., Hou, C., and Zhang, S. URDF-anything: Constructing articulated objects with 3d multimodal language model. In *The Thirty-ninth Annual Conference on Neural Information Processing Systems*, 2025b.

- Liu, J., Mahdavi-Amiri, A., and Savva, M. Paris: Part-level reconstruction and motion analysis for articulated objects. In *Proceedings of the IEEE/CVF International Conference on Computer Vision*, pp. 352–363, 2023a.
- Liu, J., Tam, H. I. I., Mahdavi-Amiri, A., and Savva, M. Cage: Controllable articulation generation. In *Proceedings of the IEEE/CVF Conference on Computer Vision and Pattern Recognition*, pp. 17880–17889, 2024a.
- Liu, J., Iliash, D., Chang, A. X., Savva, M., and Amiri, A. M. SINGAPO: Single image controlled generation of articulated parts in objects. In *The Thirteenth International Conference on Learning Representations*, 2025a.
- Liu, J., Savva, M., and Mahdavi-Amiri, A. Survey on modeling of human-made articulated objects. In *Computer Graphics Forum*, pp. e70092. Wiley Online Library, 2025b.
- Liu, M., Xu, C., Jin, H., Chen, L., Varma T, M., Xu, Z., and Su, H. One-2-3-45: Any single image to 3d mesh in 45 seconds without per-shape optimization. *Advances in Neural Information Processing Systems*, 36:22226–22246, 2023b.
- Liu, M., Shi, R., Chen, L., Zhang, Z., Xu, C., Wei, X., Chen, H., Zeng, C., Gu, J., and Su, H. One-2-3-45++: Fast single image to 3d objects with consistent multi-view generation and 3d diffusion. In *Proceedings of the IEEE/CVF conference on computer vision and pattern recognition*, pp. 10072–10083, 2024b.
- Liu, R., Wu, R., Van Hoorick, B., Tokmakov, P., Zakharov, S., and Vondrick, C. Zero-1-to-3: Zero-shot one image to 3d object. In *Proceedings of the IEEE/CVF international conference on computer vision*, pp. 9298–9309, 2023c.
- Liu, X., Zhang, J., Hu, R., Huang, H., Wang, H., and Yi, L. Self-supervised category-level articulated object pose estimation with part-level SE(3) equivariance. In *The Eleventh International Conference on Learning Representations*, 2023d.
- Liu, Y., Lin, C., Zeng, Z., Long, X., Liu, L., Komura, T., and Wang, W. Syncdreamer: Generating multiview-consistent images from a single-view image. In *The Twelfth International Conference on Learning Representations*, 2024c.
- Loshchilov, I. and Hutter, F. Decoupled weight decay regularization. In *International Conference on Learning Representations (ICLR)*, 2019.
- Mandi, Z., Weng, Y., Bauer, D., and Song, S. Real2code: Reconstruct articulated objects via code generation. In *The Thirteenth International Conference on Learning Representations*, 2025.
- Melas-Kyriazi, L., Laina, I., Rupperecht, C., Neverova, N., Vedaldi, A., Gafni, O., and Kokkinos, F. Im-3d: Iterative multiview diffusion and reconstruction for high-quality 3d generation. In *International Conference on Machine Learning (ICML)*, 2024.
- Mo, K., Zhu, S., Chang, A. X., Yi, L., Tripathi, S., Guibas, L. J., and Su, H. Partnet: A large-scale benchmark for fine-grained and hierarchical part-level 3d object understanding. In *Proceedings of the IEEE/CVF conference on computer vision and pattern recognition*, pp. 909–918, 2019.
- Mu, J., Qiu, W., Kortylewski, A., Yuille, A., Vasconcelos, N., and Wang, X. A-sdf: Learning disentangled signed distance functions for articulated shape representation. In *Proceedings of the IEEE/CVF International Conference on Computer Vision*, pp. 13001–13011, 2021.
- Pan, X., Charron, N., Yang, Y., Peters, S., Whelan, T., Kong, C., Parkhi, O., Newcombe, R., and Ren, Y. C. Aria digital twin: A new benchmark dataset for egocentric 3d machine perception. In *Proceedings of the IEEE/CVF International Conference on Computer Vision*, pp. 20133–20143, 2023.
- Peebles, W. and Xie, S. Scalable diffusion models with transformers. In *Proceedings of the IEEE/CVF International Conference on Computer Vision (ICCV)*, pp. 4195–4205, 2023.
- Robotiq Inc. Adaptive grippers. <https://robotiq.com/products/adaptive-grippers>, 2025. Accessed: 2025-02-01.
- Siddiqui, Y., Monnier, T., Kokkinos, F., Kariya, M., Kleiman, Y., Garreau, E., Gafni, O., Neverova, N., Vedaldi, A., Shapovalov, R., et al. Meta 3d assetgen: Text-to-mesh generation with high-quality geometry, texture, and pbr materials. *Advances in Neural Information Processing Systems*, 37:9532–9564, 2024.
- Siméoni, O., Vo, H. V., Seitzer, M., Baldassarre, F., Oquab, M., Jose, C., Khalidov, V., Szafraniec, M., Yi, S., Ramamonjisoa, M., Massa, F., Haziza, D., Wehrstedt, L., Wang, J., Darcet, T., Moutakanni, T., Sentana, L., Roberts, C., Vedaldi, A., Tolan, J., Brandt, J., Couprie, C., Mairal, J., Jégou, H., Labatut, P., and Bojanowski, P. Dinov3. *arXiv preprint arXiv:2508.10104*, 2025.
- Song, J., Meng, C., and Ermon, S. Denoising diffusion implicit models. In *International Conference on Learning Representations (ICLR)*, 2021.
- Tang, J., Ren, J., Zhou, H., Liu, Z., and Zeng, G. Dream-gaussian: Generative gaussian splatting for efficient 3d content creation. In *International Conference on Learning Representations (ICLR)*, 2024.

- Wagenmaker, A., Huang, K., Ke, L., Jamieson, K., and Gupta, A. Overcoming the sim-to-real gap: Leveraging simulation to learn to explore for real-world rl. *Advances in Neural Information Processing Systems*, 37:78715–78765, 2024.
- Weng, Y., Wen, B., Tremblay, J., Blukis, V., Fox, D., Guibas, L., and Birchfield, S. Neural implicit representation for building digital twins of unknown articulated objects. In *Proceedings of the IEEE/CVF Conference on Computer Vision and Pattern Recognition*, pp. 3141–3150, 2024.
- Wu, C., Li, J., Zhou, J., Lin, J., Gao, K., Yan, K., Yin, S.-m., Bai, S., Xu, X., Chen, Y., Chen, Y., Tang, Z., Zhang, Z., Wang, Z., Yang, A., Yu, B., Cheng, C., Liu, D., Li, D., Zhang, H., Meng, H., Wei, H., Ni, J., Chen, K. C., Cao, K., Peng, L., Qu, L., Wu, M., Wang, P., Yu, S., Wen, T., Feng, W., Xu, X., Wang, Y., Zhang, Y., Zhu, Y., Wu, Y., Cai, Y., and Liu, Z. Qwen-image technical report. *arXiv preprint arXiv:2508.02324*, 2025.
- Wu, T., Zhang, J., Fu, X., Wang, Y., Ren, J., Pan, L., Wu, W., Yang, L., Wang, J., Qian, C., et al. Omniobject3d: Large-vocabulary 3d object dataset for realistic perception, reconstruction and generation. In *Proceedings of the IEEE/CVF Conference on Computer Vision and Pattern Recognition*, pp. 803–814, 2023.
- Xiang, F., Qin, Y., Mo, K., Xia, Y., Zhu, H., Liu, F., Liu, M., Jiang, H., Yuan, Y., Wang, H., et al. Sapien: A simulated part-based interactive environment. In *Proceedings of the IEEE/CVF conference on computer vision and pattern recognition*, pp. 11097–11107, 2020.
- Xiang, J., Chen, X., Xu, S., Wang, R., Lv, Z., Deng, Y., Zhu, H., Dong, Y., Zhao, H., Yuan, N. J. Y., and Yang, J. Native and compact structured latents for 3d generation. *arXiv preprint arXiv:2512.14692*, 2025a.
- Xiang, J., Lv, Z., Xu, S., Deng, Y., Wang, R., Zhang, B., Chen, D., Tong, X., and Yang, J. Structured 3d latents for scalable and versatile 3d generation. In *Proceedings of the Computer Vision and Pattern Recognition Conference*, pp. 21469–21480, 2025b.
- Xu, J., Cheng, W., Gao, Y., Wang, X., Gao, S., and Shan, Y. Instantmesh: Efficient 3d mesh generation from a single image with sparse-view large reconstruction models. In *Proceedings of the European Conference on Computer Vision (ECCV)*, 2024.
- Yi, T., Fang, J., Wang, J., Wu, G., Xie, L., Zhang, X., Liu, W., Tian, Q., and Wang, X. Gaussiandreamer: Fast generation from text to 3d gaussians by bridging 2d and 3d diffusion models. In *Proceedings of the IEEE/CVF Conference on Computer Vision and Pattern Recognition*, pp. 6796–6807, 2024.
- Zhang, B., Tang, J., Niessner, M., and Wonka, P. 3dshape2vecset: A 3d shape representation for neural fields and generative diffusion models. *ACM Transactions on Graphics (TOG)*, 42(4):1–16, 2023.
- Zhang, B., Yang, T., Li, Y., Zhang, L., and Zhao, X. Compress3d: a compressed latent space for 3d generation from a single image. In *European Conference on Computer Vision*, pp. 276–292. Springer, 2024a.
- Zhang, L., Wang, Z., Zhang, Q., Qiu, Q., Pang, A., Jiang, H., Yang, W., Xu, L., and Yu, J. Clay: A controllable large-scale generative model for creating high-quality 3d assets. *ACM Transactions on Graphics (TOG)*, 43(4): 1–20, 2024b.

Appendix

This supplementary material provides additional details and results to complement the main paper. It includes the following sections:

A. Data Preparation Details

A.1. Dataset Expansion Pipeline

To enhance data diversity, we expanded the **PartNet-Mobility** dataset by converting static models from **PartNet**(Mo et al., 2019) into articulated URDF formats. The pipeline consists of:

- **Automated Synthesis:** We parsed hierarchical JSON metadata and mesh geometries to infer kinematic chains. Contact analysis was performed to determine joint types, transformation matrices, and joint limits.
- **Human-in-the-loop Verification:** All synthesized models were manually inspected to ensure physical plausibility. We specifically corrected joint axes, motion ranges, and collision mesh alignments, while discarding models with topological defects.

Meanwhile, the PhysX-3D(Cao et al., 2025a) dataset also provides dynamic URDF annotations generated from PartNet. While the dataset contains a substantial amount of high-quality data, some joint annotations are erroneous. We therefore select a subset of the dataset and manually correct the joint parameters.

A.2. Normalization

To ensure a consistent input distribution, all objects underwent the following preprocessing: We apply standard mesh preprocessing commonly used in 3D geometry pipelines. Each mesh is uniformly scaled from its original resolution while preserving aspect ratios, then translated so that the center of its axis-aligned bounding box is aligned to $(0, 0, 0)$. After normalization, the mesh is guaranteed to lie within the unit cube $[-1, 1]^3$.

A.3. Mesh Thickening

Our 3D encoding relies on the encoder from TripoSG(Li et al., 2025a), which operates on surface geometry and explicitly uses surface normals as input. However, a significant portion of meshes in PartNet and PhysX-3D are single-layer or zero-thickness surfaces. Such meshes often exhibit ill-defined or inconsistent normals, which in practice leads to unstable encoding and frequent reconstruction failures after decoding, which is shown in figure 7.

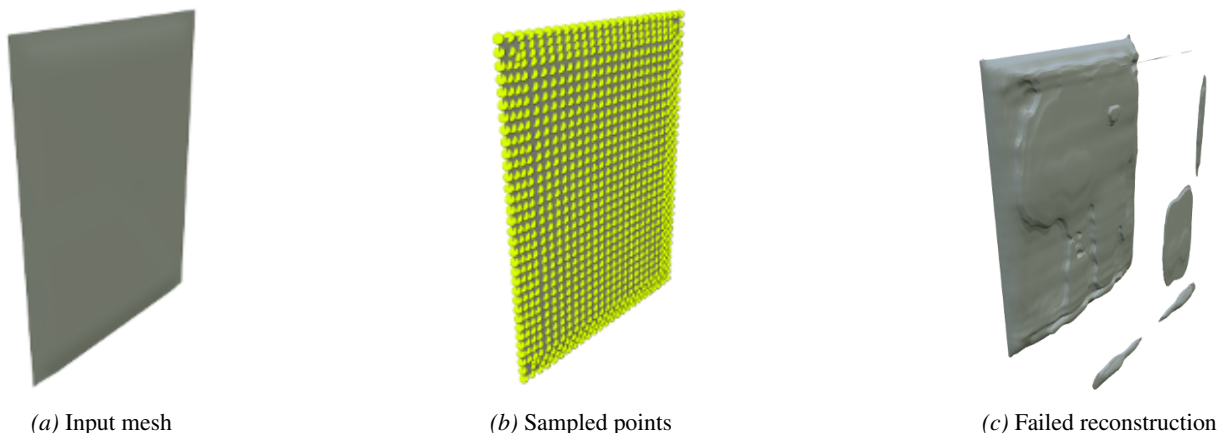


Figure 7. Failure case caused by single-layer meshes. From left to right: the input mesh, sampled surface points with unreliable normals, and the failed reconstruction after encoding and decoding.

To address this issue, we apply a mesh thickening preprocessing step to affected assets. Specifically, we convert single-layer surfaces into thin volumetric shells by offsetting the mesh along its normal direction, thereby creating a small but non-zero

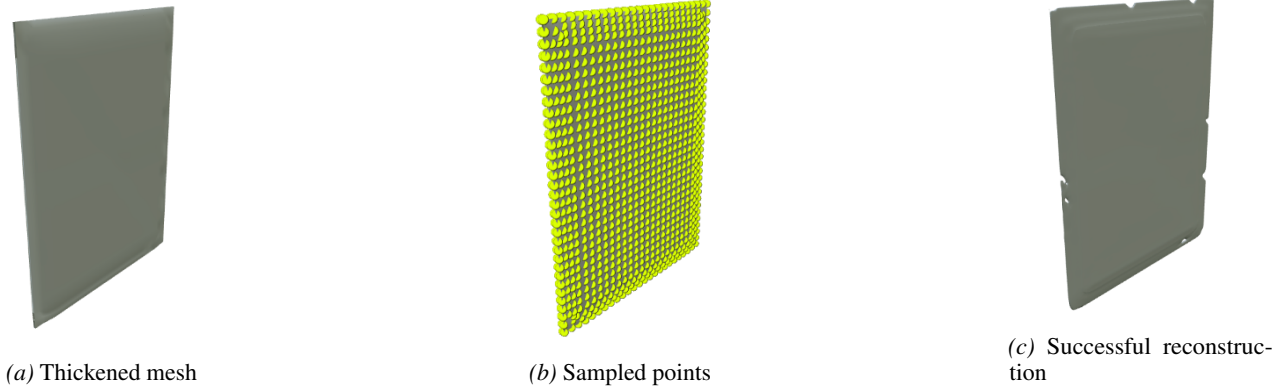


Figure 8. Effect of mesh thickening. From left to right: the thickened mesh, sampled surface points with well-defined normals, and the decoded reconstruction after encoding and decoding. Mesh thickening stabilizes normal estimation and enables reliable latent encoding.

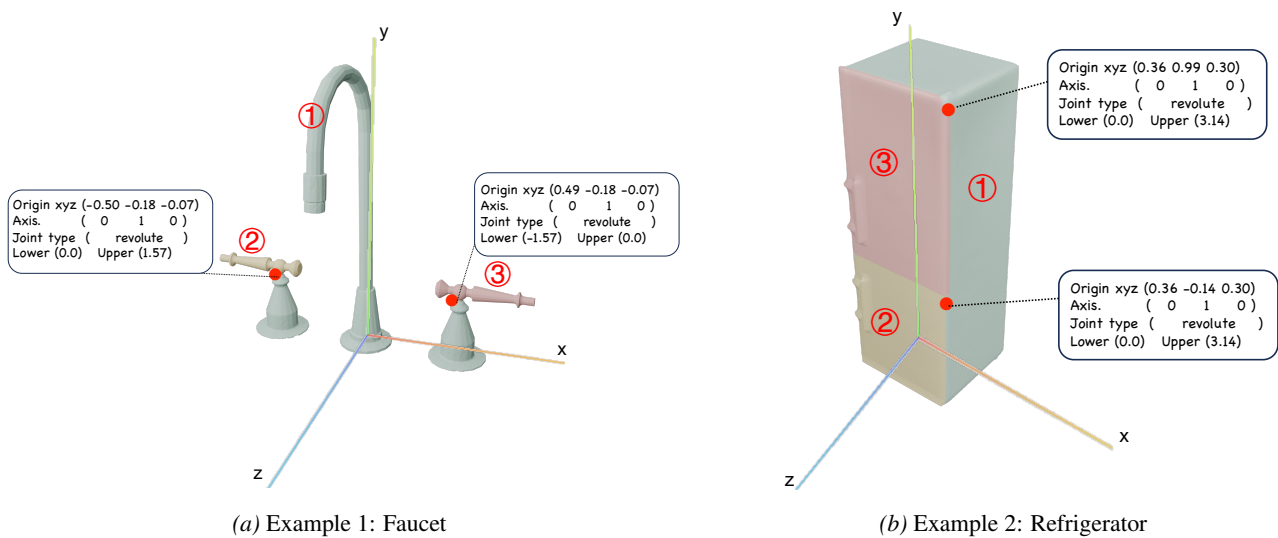


Figure 9. The visualization of link order setting

thickness. This process yields well-defined, consistently oriented normals and ensures that the encoder–decoder pipeline can reliably reconstruct the geometry, which is shown in figure 8.

As a result, the encoded 3D latents correspond to valid and stable shape representations, which is critical for both diffusion-based generation and subsequent articulated model synthesis.

A.4. Ordering of parts

Our model takes a full image and a complete 3D shape as input and does not impose any explicit constraint on the generation order. To ensure that the model outputs parts in a consistent and semantically correct sequence during autoregressive generation, the training data must follow a predefined ordering scheme.

Specifically, for articulated objects, we designate immobile components such as the base or outer frame as the first part and require the model to generate them first. For the remaining movable parts, we follow the ordering strategy of AutoPartGen(Chen et al., 2025b).

In the *automatic* setting, a fixed canonical order is used during training. All training assets are defined in a normalized canonical space, and parts are sorted lexicographically based on their axis-aligned bounding boxes: from bottom to top (Z), then left to right (X), and finally front to back (Y), following Blender’s ZXY axis convention. Concretely, parts are first compared by their minimum Z values; if these are similar, minimum X values are compared, and if still similar, minimum Y

values are used. The visualization is shown at figure 9.

The effect of this scheme is discussed in Section 5.4. Here is an example of our data format:

```
{
  "id": "258",
  "whole_image": "base.png",
  "urdf": "test.urdf",
  "links": [
    {
      "name": "link_1",
      "obj": "link_1.obj"
    },
    {
      "name": "link_3",
      "obj": "link_3.obj",
      "origin_xyz": "-0.49765583872795105 -0.17762422561645508 -0.06716569513082504",
      "axis_xyz": "0.0 1.0 0.0",
      "motion_type": "revolute",
      "lower": 0.0,
      "upper": 1.5707963267948966
    },
    {
      "name": "link_2",
      "obj": "link_2.obj",
      "origin_xyz": "0.48748037219047546 -0.1764167696237564 -0.06509745121002197",
      "axis_xyz": "0.0 1.0 0.0",
      "motion_type": "revolute",
      "lower": -1.5707963267948966,
      "upper": 0.0
    }
  ]
}
```

A.5. Rendered Images

To improve the generalization of our model to real-world visual inputs, we augment the training data with rendered images. Specifically, we leverage the open-source image editing model *Qwen-Image-Edit* (Wu et al., 2025) to transform object images from the PartNet dataset into images that more closely resemble objects observed in real-world scenes. The examples are shown in figure 10. By enhancing visual realism in terms of lighting, background, and appearance, this rendering process

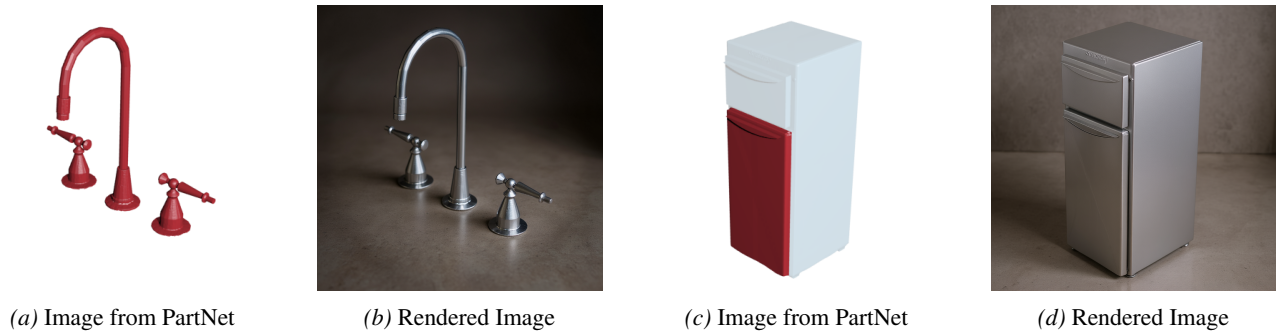


Figure 10. Examples of rendered images generated by Qwen-Image-Edit

reduces the domain gap between synthetic training data and natural images, thereby improving the robustness of our model when conditioned on input images at inference time.

B. Implementation Details

B.1. Training

3D Variational Autoencoder. We directly adopt the pretrained 3D VAE from TripoSG (Li et al., 2025a) without further training. The VAE encodes geometry using a signed distance function (SDF) representation and operates on dense surface samples. During encoding and decoding, we uniformly sample 204,800 points per shape and represent each shape using a fixed token length of 512. This pretrained VAE provides stable and high-quality 3D latent representations, which are used throughout diffusion training and inference.

Pretraining and fine-tuning. For diffusion training, we follow a two-stage strategy. We first train an image-to-3D diffusion model without URDF parameters or End-of-Token ($[EOT]$) generation. The diffusion backbone follows DiT (Peebles & Xie, 2023), consisting of 24 transformer layers with a hidden dimension of 2048. Image conditions are encoded using the DINO-v3 ViT-H/16+ model pretrained on LVD-1689M (dinov3-vith16plus-pretrain-lvd1689m), which has approximately 0.8B parameters. The geometry condition is provided by the pretrained TripoSG 3D VAE. To reduce computational cost during diffusion training, we precompute the 3D latent representations for all object parts and whole objects (denoted as $z_{pre}^{[1:k]}$ and z_{whole}) by running the 3D VAE offline, and cache the resulting latents for efficient reuse. This stage is trained for 500 epochs on 16 NVIDIA A800 GPUs.

We then fine-tune the model for an additional 100 epochs by incorporating URDF parameters and $[EOT]$ generation into the training objective. Unless otherwise specified, all other training settings, optimization strategies, and diffusion configurations remain identical to those used in the initial training stage.

Training loss configuration and hyperparameter settings During the pretraining stage, the diffusion model is optimized solely using the latent diffusion objective \mathcal{L}_{diff} defined in Eq. 5, which supervises the denoising velocity prediction in latent space. In the fine-tuning stage, we extend the training objective to jointly supervise articulated structure generation by incorporating additional losses. Specifically, the total loss is given by

$$\mathcal{L} = \mathcal{L}_{diff} + 0.1 * \mathcal{L}_{EOT} + 0.01 * \mathcal{L}_{joint},$$

where \mathcal{L}_{EOT} denotes the End-of-Token ($[EOT]$) prediction loss, and \mathcal{L}_{joint} aggregates losses for joint parameter prediction. For continuous joint parameters (e.g. joint origin, axis direction, and limits), we use ℓ_1 loss, while joint type prediction is supervised using a categorical cross-entropy loss.

Notably, for a large portion of articulated objects, the joint rotation axes are aligned with canonical directions (e.g., $(0, 0, 1)$, $(0, 1, 0)$, or $(1, 0, 0)$). In such cases, the coordinate of the joint origin along the axis direction does not affect the kinematic behavior of the joint. To avoid introducing unnecessary noise into training, we mask out the origin component along the predicted joint axis when computing the origin ℓ_1 loss. This axis-aware masking focuses supervision on the physically meaningful degrees of freedom and leads to more stable and accurate joint parameter learning.

All models are optimized using AdamW (Loshchilov & Hutter, 2019) with a learning rate of 1×10^{-5} during fine-tuning, while other optimization settings follow those used in pretraining.

B.2. Inference

At inference time, the articulated object is generated in an autoregressive manner until a termination condition is met. We explicitly introduce an End-of-Text ($[EOT]$) signal in the latent space to indicate the end of part generation. Specifically, the $[EOT]$ target is defined as a zero vector with the same dimensionality as the shape latent, i.e., a zero latent that matches the geometry latent representation.

During inference, after each autoregressive step, we measure the distance between the predicted latent and the $[EOT]$ latent. If this distance falls below a predefined threshold, the generation process is terminated, indicating that no further valid parts remain to be generated.

In addition, we incorporate a geometric redundancy check to prevent duplicate or degenerate part generation. After decoding the current part geometry, we evaluate its overlap and similarity with the previously generated part. If the overlap exceeds a predefined similarity threshold, indicating that the newly generated link is largely redundant with an existing one, the generation is also terminated.

B.3. Evaluation Metrics

We use three standard metrics to evaluate the reconstruction quality: Intersection over Union (IoU), F-score, and Chamfer Distance (CD).

Intersection over Union (IoU). IoU measures the volumetric overlap between the predicted shape P and the ground-truth shape G :

$$\text{IoU} = \frac{|P \cap G|}{|P \cup G|} \quad (13)$$

where $|\cdot|$ denotes the volume (number of occupied voxels or mesh volume) of the shape.

F-score. F-score measures the geometric similarity between two point sets P (predicted) and G (ground truth) based on a distance threshold τ . In our experiments, we set $\tau = 0.02$:

$$\text{Precision} = \frac{|\{p \in P \mid d(p, G) < \tau\}|}{|P|}, \quad (14)$$

$$\text{Recall} = \frac{|\{g \in G \mid d(g, P) < \tau\}|}{|G|}, \quad (15)$$

$$\text{F-score} = \frac{2 \cdot \text{Precision} \cdot \text{Recall}}{\text{Precision} + \text{Recall}}, \quad (16)$$

where $d(p, G) = \min_{g \in G} \|p - g\|_2$ is the distance from a predicted point to the nearest ground-truth point.

Chamfer Distance (CD). Chamfer Distance measures the average closest-point distance between two point sets:

$$\text{CD}(P, G) = \frac{1}{|P|} \sum_{p \in P} \min_{g \in G} \|p - g\|_2^2 + \frac{1}{|G|} \sum_{g \in G} \min_{p \in P} \|g - p\|_2^2 \quad (17)$$

This metric captures the overall similarity between two point clouds.

C. Visualization of Generated Shapes Across Object Categories

To qualitatively evaluate the performance of our method, we visualize the generated shapes for different object categories.

D. Limitations

While URDF-Anything+ achieves strong performance in generating articulated object models and enabling the Real-Follow-Sim pipeline, several limitations remain. First, the diversity of articulated objects in the training data is still limited. Our model primarily relies on publicly available datasets, where certain object categories contain relatively few instances. This data imbalance may restrict the model’s ability to generalize to rare or unseen articulated structures. Expanding the dataset with more diverse articulated objects and richer annotations would likely further improve performance and robustness.

Second, although our method predicts geometric structure and kinematic parameters, it does not explicitly model more complex physical properties of objects, such as mass distribution, friction, or material-dependent dynamics. As a result, some physical behaviors in simulation may not perfectly match those in the real world. Incorporating richer physical parameter estimation or physics-aware learning could further improve the fidelity of the generated digital twins.

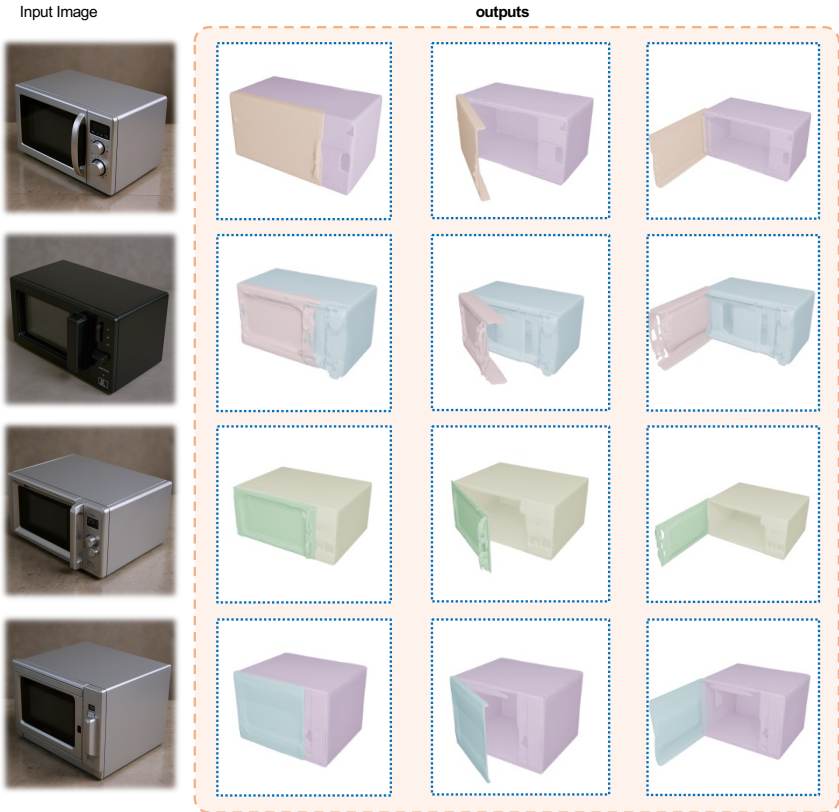


Figure 11. Generation Results of Microwaves.

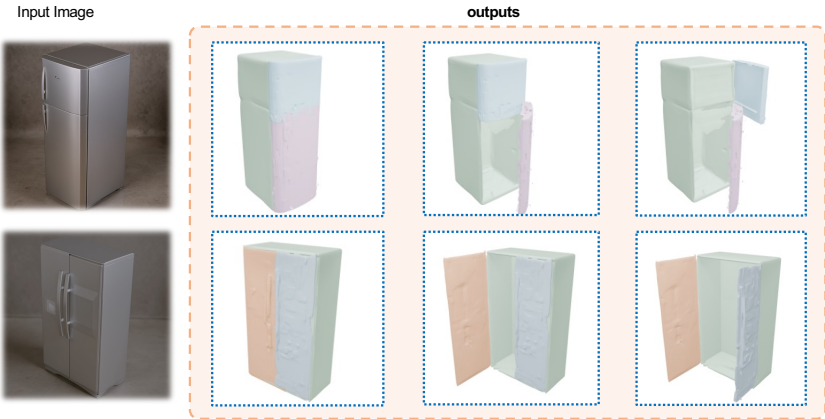


Figure 12. Generation Results of Refrigerators.

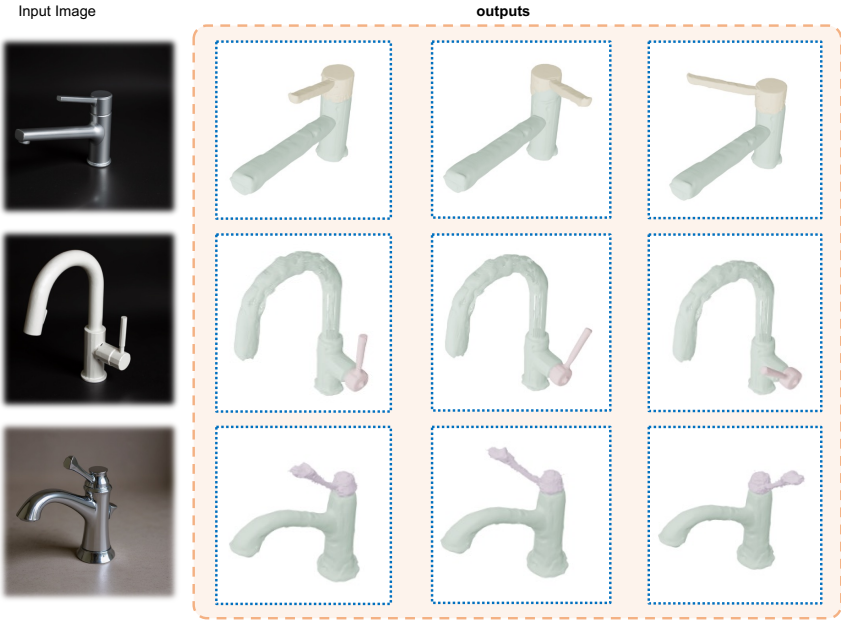


Figure 13. Generation Results of Faucets.

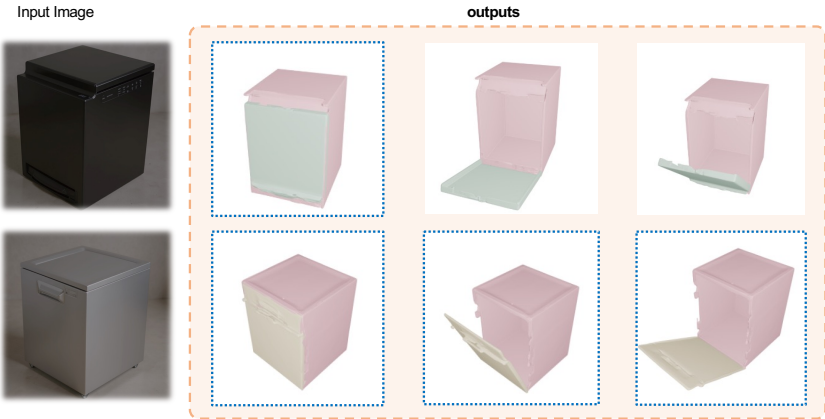


Figure 14. Generation Results of Dishwashers.